

Article

Adsorption of $\text{Cr}(\text{OH})_n^{(3-n)+}$ ($n = 1-3$) on Illite (001) and (010) Surfaces: A DFT Study

Jia Du ^{1,*}, Leilei Fan ¹, Qinghe Wang ¹ and Fanfei Min ²

¹ College of Resources and Environment, Zunyi Normal University, Zunyi 563006, China; fldxx@126.com (L.F.); wqh9746662021@163.com (Q.W.)

² Department of Materials Science and Engineering, Anhui University of Science and Technology, Huainan 232001, China; ffmin@aust.edu.cn

* Correspondence: djwell@126.com

Abstract: The development of clay adsorption materials with high Cr(III) removal capacities requires an understanding of the adsorption mechanism at the atomic level. Herein, the mechanisms for the adsorption of $\text{Cr}(\text{OH})^{2+}$, $\text{Cr}(\text{OH})_2^+$, and $\text{Cr}(\text{OH})_3$ on the (001) and (010) surfaces of illite were studied by analyzing the adsorption energies, adsorption configurations, charges, and state densities using density functional theory (DFT). The adsorption energies on the illite (010) and (001) surfaces decrease in the order: $\text{Cr}(\text{OH})^{2+} > \text{Cr}(\text{OH})_2^+ > \text{Cr}(\text{OH})_3$. In addition, the energies associated with adsorption on the (010) surface are greater than those on the (001) surface. Further, the hydrolysates are highly active and can provide adsorption sites for desorption agents. The silica (Si–O) ring on the illite (001) surface can capture $\text{Cr}(\text{OH})_n^{(3-n)+}$ ($n = 1-3$). In addition, both $\text{Cr}(\text{OH})^{2+}$ and $\text{Cr}(\text{OH})_2^+$ form one covalent bond between Cr and surface $\text{O}_{\text{S}1}$ (Cr– $\text{O}_{\text{S}1}$), whereas the hydroxyl groups of $\text{Cr}(\text{OH})_3$ form three hydrogen bonds with surface oxygens. However, increasing the number of hydroxyl groups in $\text{Cr}(\text{OH})_n^{(3-n)+}$ weakens both the covalent and electrostatic interactions between the adsorbate and the (001) surface. In contrast, the Cr in all hydrolysates can form two covalent Cr– O_{Sn} ($n = 1-2$) bonds to the oxygens on the illite (010) surface, in which Cr s and O p orbitals contribute to the bonding process. However, covalent interactions between the cation and the (010) surface are weakened as the number of hydroxyl groups in $\text{Cr}(\text{OH})_n^{(3-n)+}$ increases. These results suggest that the illite interlayer can be stripped to expose Si–O rings, thereby increasing the number of adsorption sites. Furthermore, regulating the generated Cr(III) hydrolysate can increase or weaken adsorption on the illite surface. Based on these findings, conditions can be determined for improving the adsorption capacities and optimizing the regeneration performance of clay mineral materials.

Keywords: DFT; adsorption mechanism; illite; hydroxyl chromium(III)



Citation: Du, J.; Fan, L.; Wang, Q.; Min, F. Adsorption of $\text{Cr}(\text{OH})_n^{(3-n)+}$ ($n = 1-3$) on Illite (001) and (010) Surfaces: A DFT Study. *Processes* **2021**, *9*, 2048. <https://doi.org/10.3390/pr9112048>

Academic Editors: Andrea Melchior and Suresh K. Bhatia

Received: 16 September 2021

Accepted: 9 November 2021

Published: 16 November 2021

Publisher's Note: MDPI stays neutral with regard to jurisdictional claims in published maps and institutional affiliations.



Copyright: © 2021 by the authors. Licensee MDPI, Basel, Switzerland. This article is an open access article distributed under the terms and conditions of the Creative Commons Attribution (CC BY) license (<https://creativecommons.org/licenses/by/4.0/>).

1. Introduction

Chromium pollution mainly originates from the production of products such as leather, wood preservatives, paints, and oils, as well as from processes such as electroplating, metal processing, printing, dyeing, and steel processing [1,2]. In the environment, chromium pollution is mainly found in the form of Cr(III) or Cr(VI). Although Cr(VI) is more toxic than Cr(III), when the amount of Cr(III) in red blood cells exceeds a critical threshold it can become toxic and harmful to humans [3]. Furthermore, Cr(III) can be oxidized to form the more-toxic Cr(VI), resulting in increased toxicity. Therefore, developing efficient methods for Cr(III) removal is necessary. As Cr(III) in aqueous solution exists in different chemical forms, with $\text{Cr}(\text{OH})^{2+}$, $\text{Cr}(\text{OH})_2^+$, and $\text{Cr}(\text{OH})_3$ as its main hydrolysates, understanding how to effectively remove these hydrolysates is also very important.

Adsorption methods can effectively remove chromium from water, and most studies have focused on the development of new adsorption materials [4–6]. Clay minerals have been widely adopted as adsorption materials owing to their low costs, availabilities, large specific surface areas, and strong ion exchange capacities [7,8]. Montmorillonite, kaolinite,

and illite, among others, are common clay minerals in the Earth's crust. A removal rate of up to 80.7% for Cu^{2+} from water using montmorillonite as an adsorption material has been achieved under optimized experimental conditions [9]. Furthermore, montmorillonite or kaolinite can be modified to greatly improve their adsorption capacities for heavy metals [10]. However, an understanding of the interactions between the adsorbent and the mineral surface at the atomic level is necessary to effectively modify the surface of a clay mineral.

In recent years, density functional theory (DFT) has been applied to various systems to obtain atomic-level insight and to reveal the microscopic mechanisms of adsorption processes [11]. Wang [12] studied the adsorption of Pb^{2+} on the kaolinite (001) surface using DFT, which revealed that the covalent bond between Pb and surface O has strong ionization characteristics. Peng [13] used DFT to study the adsorption of CaOH^+ on the montmorillonite (010) and (001) surfaces; their results showed that CaOH^+ can easily obtain protons from the (010) surface to form water molecules and that the interaction of the cation with the (010) surface is stronger than that with the (001) surface. Min [14] studied the adsorption of Al(III) hydrolysates on kaolinite surfaces using DFT, and found that the adsorption energies on the (010) surface decrease in the order: $\text{Al}(\text{OH})_3 > \text{Al}(\text{OH})_2^+ > \text{Al}(\text{OH})_4^-$. Such insight, obtained from DFT studies on the microscopic mechanisms of ion adsorption on the mineral surface, can provide a basis for mineral interface regulation. However, most studies have focused on montmorillonite and kaolinite, whereas illite has received considerably less attention. In illite, Al substitution for Si in the siloxane tetrahedra increases the activity of the Si–O rings and hydroxyl groups. However, the effects of these changes on the adsorption properties of illite are not well understood at the atomic level. To advance the development of illite adsorption materials, this study investigated the adsorption of $\text{Cr}(\text{OH})_2^{2+}$, $\text{Cr}(\text{OH})_2^+$, and $\text{Cr}(\text{OH})_3$ on the illite (001) and (010) surfaces using DFT. Adsorption configuration, charge, and state density were analyzed to reveal the adsorption mechanism, thereby providing a theoretical basis for the development of effective adsorption materials.

2. Computational Details

2.1. Model Construction

The initial cell configuration was derived from the illite cells constructed by Drits [15], with K ions mainly used in the interlayer to balance the cell charge. The initial crystal cell was constructed into a $2 \times 1 \times 1$ supercrystal cell. Then, Si atoms in the Si–O tetrahedra were replaced with Al atoms to afford the $\text{K}_{0.5}\text{Al}_2(\text{Si}_4\text{Al}_{0.5})\text{O}_{10}(\text{OH})_2$ chemical formula for the crystal cell. This conforms with the required lattice replacement ratio of illite. To study the microscopic adsorption mechanism of $\text{Cr}(\text{OH})_n^{(3-n)+}$ ($n = 1-3$) on different illite faces, the illite surface model was cut from the lattice body phase along the (001) surface or the (010) surface, and a 15 Å-thick vacuum layer was introduced in the direction normal to the surface of interest. All of the abovementioned models were completed using Materials Studio 2017 software.

Figure 1 shows the surface models of illite. One Si in the Si–O ring is replaced with Al, and the compensating ion (K^+) is adsorbed above the Si–O ring on the (001) surface (Figure 1a). Si atoms exposed on the (010) surface coordinate with OH to form $\equiv\text{Si}-\text{OH}$, and Al atoms coordinate with OH to form $\equiv\text{Al}-\text{OH}$ or $\equiv\text{Al}-(\text{OH})(\text{OH}_2)$ (Figure 1b) [16]. The Al atom was chosen to coordinate with OH to form $\equiv\text{Al}-\text{OH}$ on the (010) surface in the model. The illite (001) and (010) surface models were constructed with 82 and 94 atoms, respectively.

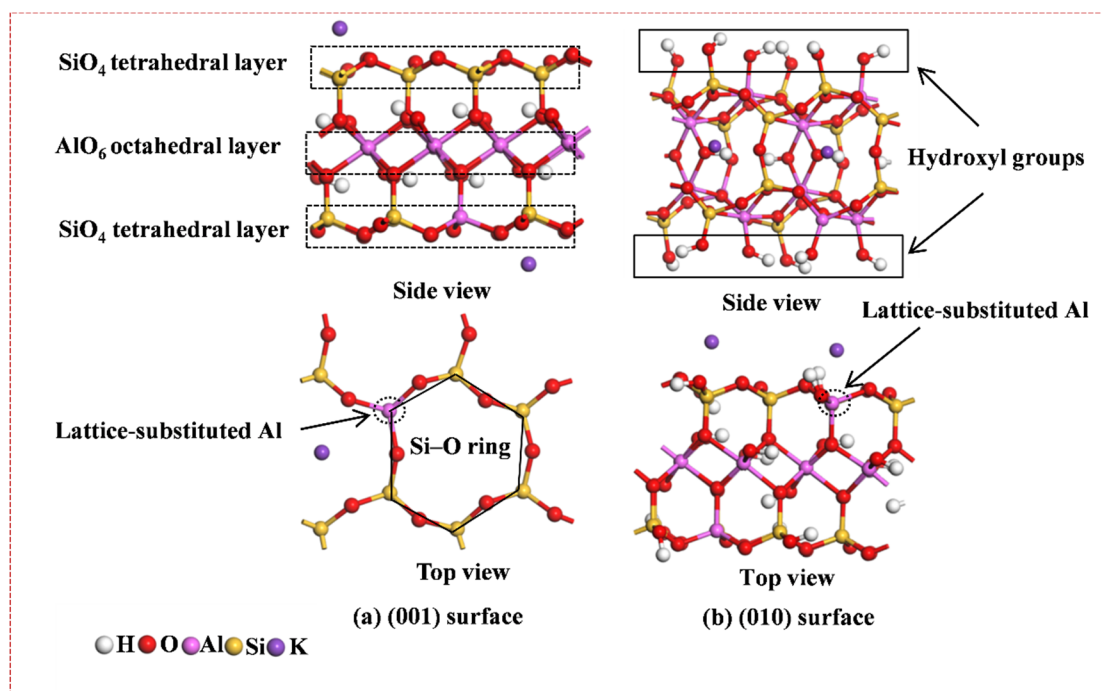


Figure 1. Structures of illite surfaces: (a) (001) surface and (b) (010) surface.

2.2. Calculation Method

The DFT-based CASTEP module [17,18] in Materials Studio 2017 was used to optimize the structure of the illite supercell, and the generalized gradient approximation (GGA) with the Perdew–Burke–Ernzerhof (PBE) exchange correlation function was applied in the optimizations [19]. The DFT-D2 dispersion correction method of Grimme was used to calculate DFT energies [20]. The plane-wave cutoff energy was 400 eV, and the atomic positions were optimized using the Broyden–Fletcher–Goldfarb–Shanno (BFGS) algorithm until the displacement, force, and total energy converged to less than $1 \times 10^{-3} \text{ \AA}$, $3 \times 10^{-2} \text{ eV/\AA}$, and $1 \times 10^{-5} \text{ eV/atom}$, respectively. Brillouin zone [21] integrations with $(3 \times 2 \times 1)$ k-point grids were carried out on the illite supercell. The optimized parameters of the illite supercell ($2 \times 1 \times 1$) are $a = 10.42 \text{ \AA}$, $b = 8.99 \text{ \AA}$, $c = 10.15 \text{ \AA}$, $\alpha = 89.95^\circ$, $\beta = 102.33^\circ$, and $\gamma = 89.97^\circ$, which are very similar to the experimental values ($a = 10.40 \text{ \AA}$, $b = 8.95 \text{ \AA}$, $c = 10.18 \text{ \AA}$, $\alpha = 90.00^\circ$, $\beta = 101.68^\circ$, and $\gamma = 90.00^\circ$) [15]. The surface models were optimized using an exchange correlation function, cutoff energy, and convergence criteria consistent with the illite supercell. Considering the influence of calculation time and ion polarization, the k-point grids were limited to Γ , and spin polarization was incorporated into the calculations. Before being adsorbed on the illite surface, $\text{Cr(OH)}_n^{(3-n)+}$, Cr(OH)_2^+ , and Cr(OH)_3 were optimized in a $15 \times 15 \times 15 \text{ \AA}^3$ cubic box using optimization standards consistent with those for the surface models. The valence electrons selected for the pseudopotential calculation of the atoms in the simulation were Si $3s^2 3p^2$, Al $3s^2 3p^1$, Cr $3d^5 4s^1$, O $2s^2 2p^4$, H $1s^1$, and K $4s^1$.

2.3. Calculation of Adsorption Energy

The strength of the $\text{Cr(OH)}_n^{(3-n)+}$ ($n = 1\text{--}3$) adsorption at each site on the surface was analyzed by calculating the adsorption energy. The adsorption energy on the illite surface can be calculated using the following formula:

$$E_{\text{ads}} = E[\text{Cr(OH)}_n^{(3-n)+} - \text{illite}] - E[\text{illite}] - E[\text{Cr(OH)}_n^{(3-n)+}] \quad (1)$$

where $E[\text{Cr(OH)}_n^{(3-n)+} - \text{illite}]$ represents the total energy of the adsorbed system, $E[\text{illite}]$ is the energy of the illite surface model, $E[\text{Cr(OH)}_n^{(3-n)+}]$ is the energy of $\text{Cr(OH)}_n^{(3-n)+}$,

and E_{ads} is the adsorption energy of $\text{Cr}(\text{OH})_n^{(3-n)+}$ on the surface. A negative value indicates that the adsorption of $\text{Cr}(\text{OH})_n^{(3-n)+}$ on the surface is an exothermic process, meaning that the reaction is spontaneous. Further, a larger E_{ads} value corresponds to a more stable adsorption configuration. In contrast, a positive value corresponds to an endothermic process, indicating that adsorption is not spontaneous and the adsorption configuration is unstable.

3. Results and Discussion

3.1. Adsorption Geometries on the Illite (001) Surface

The DFT-simulated optimal adsorption configurations of $\text{Cr}(\text{OH})_n^{(3-n)+}$, $\text{Cr}(\text{OH})_2^+$, and $\text{Cr}(\text{OH})_3$ on the illite (001) surface are shown in Figure 2, with the calculated energy characteristics and structural parameters listed in Table 1. The adsorption energies of $\text{Cr}(\text{OH})_n^{(3-n)+}$, $\text{Cr}(\text{OH})_2^+$, and $\text{Cr}(\text{OH})_3$ on the illite (001) surface are -235.78 , -128.36 , and -78.89 kJ/mol, respectively. In contrast, the adsorption energies of water molecules on the illite (001) surface vary from -48 to 57.6 kJ/mol [22]. Therefore, we can infer that $\text{Cr}(\text{OH})_n^{(3-n)+}$ displaces water molecules to adsorb preferentially on the (001) surface. The adsorption energy of $\text{Cr}(\text{OH})_n^{(3-n)+}$ on the (001) surface decreases with an increasing number of hydroxyl groups. However, further analyses of the adsorption configurations are required to understand the origin of this change in adsorption energy.

The $\text{Cr}\cdots\text{O}_{\text{Sn}}$ ($n = 2-6$) atomic distances range from 3.054 to 4.381 Å in the I(001)– $\text{Cr}(\text{OH})_n^{(3-n)+}$ configuration, and a 2.152 Å-long covalent bond with a Mulliken bond population of 0.04 formed between Cr and O_{S1} , which is near the substituted Al atom. On the other hand, the $\text{Cr}\cdots\text{O}_{\text{Sn}}$ ($n = 2-6$) atomic distances range from 2.987 to 4.451 Å in the I(001)– $\text{Cr}(\text{OH})_2^+$ configuration, and a 2.185 Å-long covalent bond with a Mulliken bond population of 0.02 formed between Cr and O_{S1} . $\text{Cr}(\text{OH})_3$ is adsorbed above the center of the Si–O ring through hydrogen bonds between H_n ($n = 1-3$) and O_{Sn} ($n = 2, 4, 6$) that are $1.829-1.996$ Å long. The $\text{Cr}\cdots\text{O}_{\text{Sn}}$ ($n = 1-6$) atomic distances range from 3.597 to 4.049 Å for the I(001)– $\text{Cr}(\text{OH})_3$ configuration.

The $\text{Cr}(\text{OH})_n^{(3-n)+}$ species are adsorbed above the Si–O ring on the (001) surface. The Cr in $\text{Cr}(\text{OH})_n^{(3-n)+}$ or $\text{Cr}(\text{OH})_2^+$ forms a covalent bond with O_{S1} owing to the strong electrostatic potential energy above the Si–O ring, as Al substitution enhances the activity of the surrounding oxygen atoms [22–25]. Therefore, the Si–O ring captures such a cation to form a covalent Cr– O_{S1} bond. In contrast, the hydrogen bonds between the hydroxyl groups of $\text{Cr}(\text{OH})_3$ and surface oxygens increase the distance between Cr and the (001) surface. This hinders the formation of a covalent bond between Cr and O_{S1} . The covalent Cr– O_{S1} bond becomes longer and its Mulliken bond populations decrease with an increasing number of hydroxyl groups in $\text{Cr}(\text{OH})_n^{(3-n)+}$. This weakens the covalent interaction between the adsorbate and the surface.

3.2. Adsorption Geometries on the Illite (010) Surface

The DFT-simulated optimal adsorption configurations of $\text{Cr}(\text{OH})_n^{(3-n)+}$, $\text{Cr}(\text{OH})_2^+$, and $\text{Cr}(\text{OH})_3$ on the illite (010) surface are shown in Figure 3, with calculated energy characteristics and structural parameters listed in Table 2. The adsorption energies for water molecules on the (010) surface of the clay mineral are $30.7-82.6$ kJ/mol [26], whereas those of $\text{Cr}(\text{OH})_n^{(3-n)+}$, $\text{Cr}(\text{OH})_2^+$, and $\text{Cr}(\text{OH})_3$ are -348.18 , -282.20 , and -206.63 kJ/mol, respectively. This indicates that the hydrolyzed products can displace water molecules to adsorb preferentially on the (010) surface.

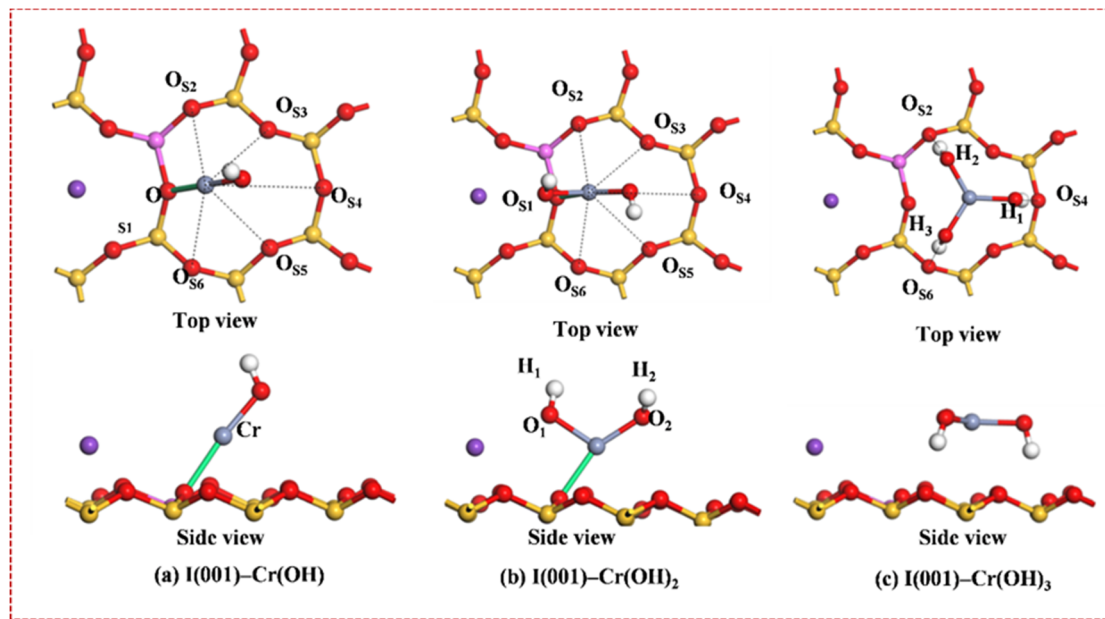


Figure 2. Stable configurations of $\text{Cr(OH)}_n^{(3-n)+}$ adsorbed on the illite (001) surface.

Table 1. Calculated energy characteristics (kJ/mol) and structural parameters (Å) of $\text{Cr(OH)}_n^{(3-n)+}$ adsorbed on the illite (001) surface.

Mode	$\text{O}_{S1}-\text{Cr}$	$\text{O}_{S_n}\cdots\text{Cr}$	$\text{O}_S\cdots\text{H}$	$\text{Cr}-\text{O}_{\text{Cr(OH)}_n}$	E_{ads} (kJ/mol)
I(001)-Cr(OH)	2.152 [0.04]	3.054–4.381, n = 2–6	-	1.904 (1.792)	-235.78
I(001)-Cr(OH) ₂	2.185 [0.02]	2.987–4.451, n = 2–6	-	1.834–1.9, 114.007 (1.759–1.757, 156.006) 1.776–1.832,	-128.36
I(001)-Cr(OH) ₃	-	3.597–4.049, n = 1–6	1.829–1.996	117.551–121.617 (1.789–1.787, 119.304–120.719)	-78.89

The $\text{Cr}-\text{O}_{\text{Cr(OH)}_n}$ column lists the $\text{Cr}-\text{O}$ bond lengths (Å) and $\text{O}-\text{Cr}-\text{O}$ bond angles ($^\circ$) of adsorbed $\text{Cr(OH)}_n^{(3-n)+}$, with the corresponding configuration parameters of $\text{Cr(OH)}_n^{(3-n)+}$ before adsorption given in parentheses. The values in square brackets are Mulliken bond populations.

Cr and O_{S_n} ($n = 1-2$) form covalent bonds that are 2.050 and 2.064 Å long, respectively, in the I(010)-Cr(OH) configuration, with Mulliken bond populations of 0.18 and 0.13, respectively. Further, O_1 and H_{S_n} ($n = 1-2$) form hydrogen bonds that are 1.615 Å and 1.975 Å long, respectively. On the other hand, Cr and O_{S_n} ($n = 1-2$) form covalent bonds with lengths 2.053 and 2.111 Å, respectively, in the I(010)-Cr(OH)₂ configuration, with Mulliken bond populations of 0.14 and 0.07, respectively. In addition, a 1.5965 Å-long hydrogen bond is formed between O_1 and H_{S1} . On the other hand, Cr and O_{S_n} ($n = 1-2$) form covalent bonds that are 2.088 and 2.157 Å long, respectively, in the I(010)-Cr(OH)₃ configuration, with Mulliken bond populations of 0.09 and 0.04, respectively. In addition, O_1 and H_{S_n} ($n = 1-2$) form hydrogen bonds of lengths 1.638 and 1.810 Å, respectively.

Thus, $\text{Cr(OH)}_n^{(3-n)+}$ ($n = 1-3$) adsorbed on the (010) surface forms a chelate complex, with covalent bonds between Cr and $\equiv\text{Al}_{\text{IV}}-\text{O}$ in the SiO_4 tetrahedral layer and $\equiv\text{Al}_{\text{V}}-\text{O}$ in the AlO_6 octahedral layer. Cr interacts preferentially with $\equiv\text{Al}_{\text{IV}}-\text{O}$ and $\equiv\text{Al}_{\text{V}}-\text{O}$, as their pKa values are higher than those of the other hydroxyl groups [27]. The $\text{Cr}-\text{O}_{S_n}$ ($n = 1-2$) bonds lengthen and their Mulliken bond populations decrease with an increasing number of hydroxyl groups in $\text{Cr(OH)}_n^{(3-n)+}$. This weakens the covalent bond and reduces the adsorption energy. The $\text{Cr}-\text{O}$ bond lengths and $\text{O}-\text{Cr}-\text{O}$ bond angles in $\text{Cr(OH)}_n^{(3-n)+}$ are different following adsorption on the (001) or (010) surface (Tables 1 and 2). This indicates that the adsorbates exhibit some activity.

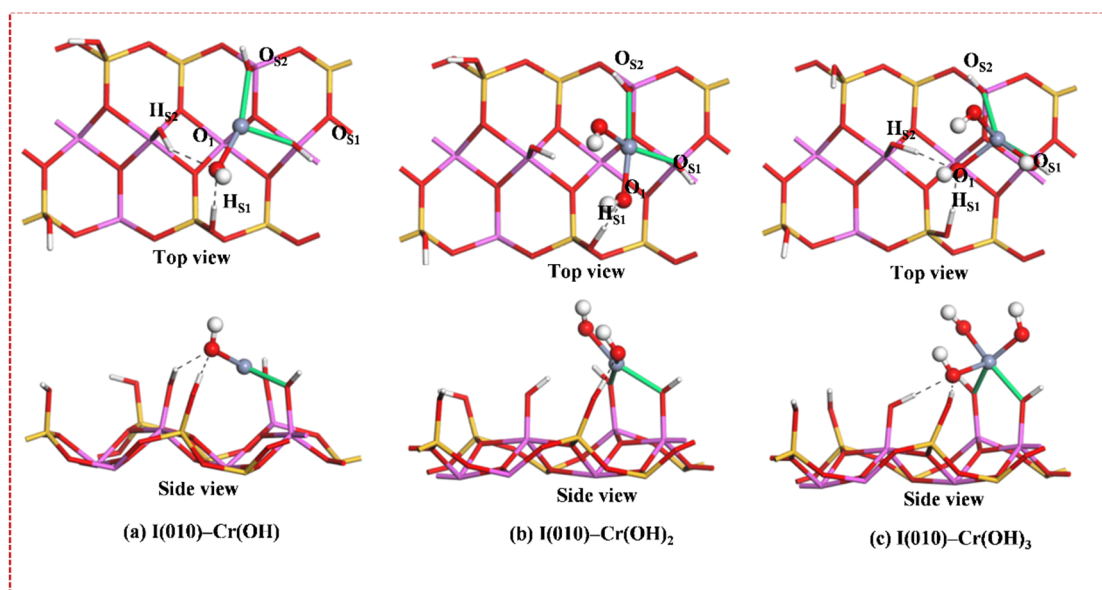


Figure 3. Stable configurations of $\text{Cr(OH)}_n^{(3-n)+}$ adsorbed on the illite (010) surface.

Table 2. Calculated energy characteristics (kJ/mol) and structural parameters (Å) of $\text{Cr(OH)}_n^{(3-n)+}$ adsorbed on the illite (010) surface.

Mode	$\text{O}_{\text{S}1}\text{-Cr}$	$\text{O}_{\text{S}2}\text{-Cr}$	$\text{O}_1\cdots\text{H}_5$	$\text{Cr-O}_{\text{Cr(OH)}_n}$	E_{ads} (kJ/mol)
I(010)-Cr(OH)	2.050 [0.18]	2.064 [0.13]	1.615–1.975	1.904 (1.792)	−348.18
I(010)-Cr(OH) ₂	2.053 [0.14]	2.111 [0.07]	1.596	1.839–1.916, 98.771 (1.757–1.759, 156.006)	−282.20
I(010)-Cr(OH) ₃	2.088 [0.09]	2.157 [0.04]	1.638–1.810	96.842–111.035 (1.789–1.787, 119.304–120.719)	−206.63

The $\text{Cr-O}_{\text{Cr(OH)}_n}$ column lists the Cr–O bond lengths (Å) and O–Cr–O bond angles ($^\circ$) of adsorbed $\text{Cr(OH)}_n^{(3-n)+}$, with the corresponding configuration parameters of $\text{Cr(OH)}_n^{(3-n)+}$ before adsorption given in parentheses. The values in square brackets are Mulliken bond populations.

3.3. Charge Analysis

The Si–O ring on the illite (001) surface, which has a low electrostatic potential energy and is strongly electronegative, can trap cations. The charge distributions in the stable adsorption configurations of $\text{Cr(OH)}_n^{(3-n)+}$ on the (001) surface can be obtained by analyzing electron density differences. To ensure the feasibility and validity of the DFT method, initial configurations of $\text{Cr(OH)}_n^{(3-n)+}$ and uncharged illite surfaces were simulated [28–30]. Figure 4 shows the differences in electron density for Cr(OH)^{2+} , Cr(OH)_2^+ , and Cr(OH)_3 adsorbed on the illite (001) surface. Electron density overlap between Cr and $\text{O}_{\text{S}1}$ in the I(001)-Cr(OH), and I(001)-Cr(OH)₂ configurations is observed. This is due to the existence of covalent bonds and is in accordance with the previous results. Both Cr and $\text{O}_{\text{S}n}$ ($n = 2\text{--}6$) show accumulation and loss of charge, indicative of an electron transfer between them. In addition, charge accumulation and loss between $\text{O}_{\text{S}1}$ from Cr(OH)_2^+ and the equilibrium K ion are observed in the I(001)-Cr(OH)₂ configuration, indicative of an electron transfer between Cr(OH)_2^+ and K. Electron transfer between Cr and $\text{O}_{\text{S}n}$ ($n = 1\text{--}6$) is observed in the I(001)-Cr(OH)₃ configuration, but more electron transfers are observed between $\text{O}_{\text{S}n}$ ($n = 2, 4, \text{ and } 6$) and H_n ($n = 1\text{--}3$) owing to the existence of hydrogen bonds.

To further analyze the charge distribution, the atomic populations/charges of Cr(OH)^{2+} , Cr(OH)_2^+ , and Cr(OH)_3 before and after adsorption on the illite (001) surface and changes in the charges of the adsorbates and surfaces were determined, as summarized in Table 3. $\text{O}_{\text{S}n}$ loses 0.01e–0.06e through adsorption of Cr(OH)^{2+} on the (001) surface, whereas Cr(OH)^{2+}

gains 0.09e from the surface. O_{Sn} loses 0.01e–0.06e and K gains 0.08e from the surface by the adsorption of $Cr(OH)_2^+$ on the (001) surface, while $Cr(OH)_2^+$ loses 0.03e to the surface, and the adsorption of $Cr(OH)_3$ on the (001) surface results in O_{Sn} losing 0.01e–0.02e and $Cr(OH)_3$ gaining 0.01e from the surface. Thus, the degree of electron transfer decreases with an increasing number of hydroxyl groups in $Cr(OH)_n^{(3-n)+}$, indicative of weakened electrostatic interactions between the adsorbates and the surface.

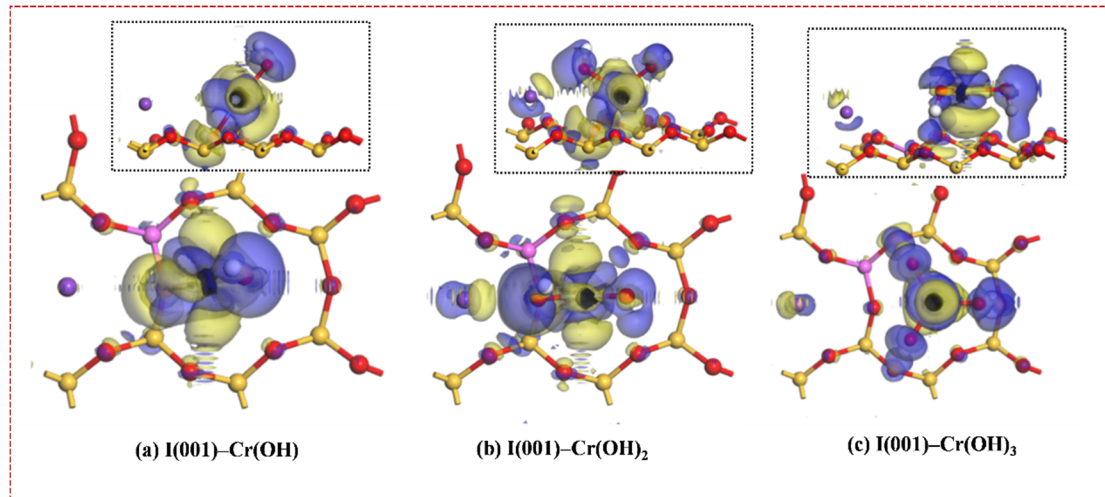


Figure 4. Electron density differences for $Cr(OH)_2^+$, $Cr(OH)_2^+$, and $Cr(OH)_3$ adsorbed on the illite (001) surface. The blue and yellow areas indicate increases and decreases in electron density, respectively. The isovalue is $0.008 e/\text{\AA}^3$.

Table 3. Atomic populations/charges of $Cr(OH)_2^+$, $Cr(OH)_2^+$, and $Cr(OH)_3$ before and after adsorption on the illite (001) surface, and changes in hydrolysate and surface charges.

Model	Name	Before					After				
		s	p	d	Total	Charge/e	s	p	d	Total	Charge/e
I(001)- Cr(OH)	O _{S1}	1.86	5.34	0	7.2	−1.2	1.85	5.29	0	7.14	−1.14
	O _{S2}	1.87	5.31	0	7.18	−1.18	1.87	5.29	0	7.16	−1.16
	O _{S3}	1.85	5.29	0	7.14	−1.14	1.85	5.28	0	7.13	−1.13
	O _{S4}	1.84	5.34	0	7.18	−1.18	1.84	5.33	0	7.17	−1.17
	O _{S5}	1.85	5.28	0	7.14	−1.14	1.85	5.27	0	7.13	−1.13
	O _{S6}	1.85	5.28	0	7.13	−1.13	1.85	5.27	0	7.12	−1.12
	Cr	2.84	6.16	4.51	13.5	0.51	2.63	6.19	4.73	13.55	0.45
	H	0.58	0	0	0.58	0.42	0.6	0	0	0.6	0.4
	O	1.88	5.05	0	6.93	−0.93	1.88	5.06	0	6.94	−0.94
	I(001)					0				+0.09	
	Cr(OH) ₂ ²⁺					0				−0.09	
I(001)- Cr(OH) ₂	K	1.97	5.88	0	7.85	1.15	2.05	5.88	0	7.93	1.07
	O _{S1}	1.86	5.34	0	7.2	−1.2	1.85	5.29	0	7.14	−1.14
	O _{S2}	1.87	5.31	0	7.18	−1.18	1.87	5.29	0	7.16	−1.16
	O _{S3}	1.85	5.29	0	7.14	−1.14	1.85	5.28	0	7.13	−1.13
	O _{S4}	1.84	5.34	0	7.18	−1.18	1.84	5.32	0	7.16	−1.16
	O _{S5}	1.85	5.28	0	7.14	−1.14	1.85	5.27	0	7.13	−1.13
	O _{S6}	1.85	5.28	0	7.13	−1.13	1.85	5.27	0	7.12	−1.12
	Cr	2.49	6.12	4.51	13.12	0.88	2.42	6.14	4.48	13.04	0.96
	H ₁	0.52	0	0	0.52	0.48	0.59	0	0	0.59	0.41
	H ₂	0.52	0	0	0.52	0.48	0.59	0	0	0.59	0.41
	O ₁	1.86	5.07	0	6.92	−0.92	1.88	5.02	0	6.9	−0.9
O ₂	1.85	5.07	0	6.92	−0.92	1.89	4.97	0	6.85	−0.85	

Table 3. Cont.

Model	Name	Before					After				
		s	p	d	Total	Charge/e	s	p	d	Total	Charge/e
	I(001) Cr(OH) ₂ ⁺					0					−0.03
						0					0.03
I(001)- Cr(OH) ₃	O _{S1}	1.86	5.34	0	7.2	−1.2	1.86	5.33	0	7.19	−1.19
	O _{S2}	1.87	5.31	0	7.18	−1.18	1.87	5.3	0	7.16	−1.16
	O _{S3}	1.85	5.29	0	7.14	−1.14	1.85	5.28	0	7.13	−1.13
	O _{S4}	1.84	5.34	0	7.18	−1.18	1.84	5.32	0	7.16	−1.16
	O _{S5}	1.85	5.28	0	7.14	−1.14	1.85	5.28	0	7.13	−1.13
	O _{S6}	1.85	5.28	0	7.13	−1.13	1.85	5.27	0	7.12	−1.12
	Cr	2.27	6.09	4.38	12.74	1.26	2.29	6.19	4.39	12.87	0.99
	H ₁	0.55	0	0	0.55	0.45	0.64	0	0	0.64	0.36
	H ₂	0.55	0	0	0.55	0.45	0.59	0	0	0.59	0.36
	H ₃	0.55	0	0	0.55	0.45	0.58	0	0	0.58	0.35
	O ₁	1.88	4.99	0	6.87	−0.87	1.87	4.98	0	6.84	−0.73
	O ₂	1.89	4.99	0	6.87	−0.87	1.86	4.94	0	6.81	−0.67
	O ₃	1.88	4.99	0	6.87	−0.87	1.87	4.95	0	6.82	−0.67
	I(001) Cr(OH) ₃					0					0.01
						0					−0.01

3.4. State Density Analysis

Heavy metal ions usually interact with the hydroxyl groups on the illite (010) surface through covalent bonds. To further clarify the bonding mechanism between Cr(OH)_n^{(3−n)+} and the surface hydroxyl groups, we analyzed the partial densities of states (PDOSs) of the Cr(OH)_n^{(3−n)+}/illite geometries. Figure 5 shows the PDOSs of the Cr–O_{S1} bonds formed after Cr(OH)_n^{(3−n)+} adsorption on the illite surfaces, where the Fermi energy is set to zero. Covalent interactions can be identified by PDOS intensities from different orbitals within the same energy range [31].

As shown in Figure 5a–c, Cr(OH)²⁺, Cr(OH)₂⁺, and Cr(OH)₃ adsorbed on the illite (010) surface show similar Cr–O_{S1} bonding PDOSs. The surface O_{S1} p and Cr s orbitals participate in bonding at −3 to −10 eV, with the O_{S1} p orbital dominating. The s orbital of Cr and the p orbital of O_{S1} also participate in antibonding in the 1 to 10 eV range. Cr–O_{S1} bond formation is favorable, as the bonding mode is greater than the antibonding mode. However, as shown in Figure 5d, the O_{S1} p and Cr s orbitals participate in bonding in the −1.5 to −8 eV range and antibonding in the 0.5 to 7.5 eV range when Cr(OH)²⁺ is adsorbed on the illite (001) surface; hence, weaker bonding modes and stronger antibonding modes are observed compared with Cr–O_{S1} bonding on the (010) surface. This result indicates that the covalent Cr–O_{S1} bond on the (001) surface is weaker than that on the (010) surface, which is consistent with the bond length and population results. The Cr s, d and O p orbitals exhibit peaks at the Fermi level, which indicates that the adsorbates are strongly active, which is consistent with the adsorption configuration analyses. Thus, adsorption sites are provided for the desorption agents, enabling them to interact with Cr(OH)_n^{(3−n)+} and repelling them from the surface, thereby restoring the adsorption capacity of the surface.

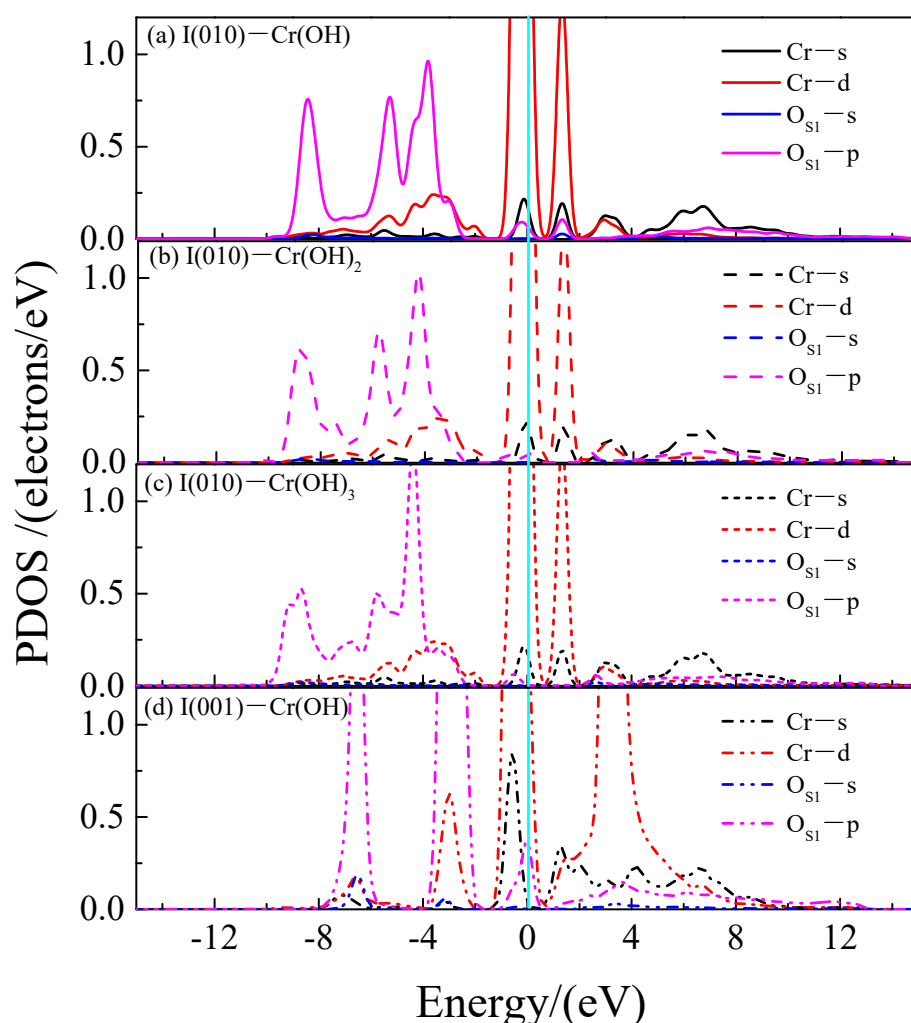


Figure 5. $\text{Cr(OH)}_n^{(3-n)+}$ PDOSs of surface O_{S1} and Cr: (a) I(010)-Cr(OH) , (b) I(010)-Cr(OH)_2 , (c) I(010)-Cr(OH)_3 , and (d) I(001)-Cr(OH) .

4. Conclusions

To clarify the mechanism for the adsorption of Cr(III) hydrolysates on illite at the atomic level, we investigated the adsorptions of $\text{Cr(OH)}_n^{(3-n)+}$ ($n = 1-3$) on the illite (001) and (010) surfaces using DFT. The following conclusions are drawn based on adsorption configuration, charge, and PDOS analyses.

1. The adsorption energies of $\text{Cr(OH)}_n^{(3-n)+}$ ($n = 1-3$) on the (010) and (001) surfaces of illite decrease in the order $\text{Cr(OH)}_2^{2+} > \text{Cr(OH)}_3 > \text{Cr(OH)}_1^{3+}$, with adsorption energies on the (010) surface greater than those on the (001) surface. The hydrolysates are strongly active and can provide adsorption sites for desorption agents.

2. The Si-O ring on the (001) illite surface can capture $\text{Cr(OH)}_n^{(3-n)+}$, Cr(OH)_2^{2+} , and Cr(OH)_1 through the formation of one (Cr-O_{S1}) covalent bond and three hydrogen bonds involving the hydroxyl groups of Cr(OH)_3 and surface oxygens. However, the covalent and electrostatic interactions between the adsorbate and the (001) surface weaken with an increasing number of hydroxyl groups in $\text{Cr(OH)}_n^{(3-n)+}$.

3. $\text{Cr(OH)}_n^{(3-n)+}$ can form two covalent bonds on the illite (010) surface (Cr-O_{S1} ($n = 1-2$)) to $\equiv\text{Al}_{\text{IV}}\text{-O}_{\text{S1}}$ and $\equiv\text{Al}_{\text{VI}}\text{-O}_{\text{S2}}$, with the Cr s and O p orbitals contributing to this bonding process. These covalent interactions between the adsorbate and the (010) surface are weakened by increasing the number of hydroxyl groups in $\text{Cr(OH)}_n^{(3-n)+}$.

4. The results of this study suggest that the illite interlayer can be stripped to expose the silica rings, thereby increasing the number of adsorption sites. Furthermore, the generated Cr(III) hydrolysates can be regulated to increase or decrease adsorption on the

illite surfaces. These findings provide potential strategies for improving the adsorption capacities and optimizing the regeneration performance of clay mineral materials.

Author Contributions: Conceptualization, J.D. and L.F.; methodology, J.D. and F.M.; software, J.D. and F.M.; investigation, L.F.; data curation, J.D.; writing—original draft preparation, Q.W.; writing—review and editing, J.D.; supervision, J.D. All authors have read and agreed to the published version of the manuscript.

Funding: This research was supported by Guizhou Provincial Natural Science Foundation (No. Qian Ke He Ji Chu—ZK[2021] Yi Ban 259), Guizhou Education Department Youth Science and Technology Talents Growth Project (No. Qian Jiao He KY Zi [2019]111) and Doctoral Foundation Project of Zunyi Normal University (No. Zun Shi BS [2019] 35).

Conflicts of Interest: The authors declare no conflict of interest.

References

1. Aravindhan, R.; Madhan, B.; Rao, J.R.; Narir, B.U.; Ramasami, T. Bioaccumulation of chromium from tannery wastewater: An approach for chrome recovery and reuse. *Environ. Sci. Technol.* **2004**, *1*, 300–306. [\[CrossRef\]](#)
2. Sudha Bai, R.T.E.A. Biosorption of Cr (VI) from aqueous solution by rhizopus nigricans. *Bioresour. Technol.* **2001**, *79*, 73–81.
3. Suwalsky, M.; Castro, R.; Villena, F.; Sotomayor, C. Cr(III) exerts stronger structural effects than Cr(VI) on the human erythrocyte membrane and molecular models. *J. Inorg. Biochem.* **2008**, *102*, 842–849. [\[CrossRef\]](#)
4. Pan, J.; Jiang, J.; Xu, R. Adsorption of Cr(III) from acidic solutions by crop straw derived biochars. *J. Environ. Sci.* **2013**, *25*, 1957–1965. [\[CrossRef\]](#)
5. Li, Y.; Liu, C.; Chou, C. Adsorption of Cr(III) from wastewater by wine processing waste sludge. *J. Colloid Interf. Sci.* **2004**, *273*, 95–101. [\[CrossRef\]](#) [\[PubMed\]](#)
6. Gode, F.; Pehlivan, E. Adsorption of Cr(III) ions by Turkish brown coals. *Fuel Process. Technol.* **2005**, *86*, 875–884. [\[CrossRef\]](#)
7. Uddin, M.K. A review on the adsorption of heavy metals by clay minerals, with special focus on the past decade. *Chem. Eng. J.* **2017**, *308*, 438–462. [\[CrossRef\]](#)
8. Arnfalk, P.; Wasay, S.A.; Tokunaga, S. A comparative study of Cd, Cr(III), Cr(VI), Hg, and Pb uptake by minerals and soil materials. *Water Air Soil Pollut.* **1996**, *87*, 131–148. [\[CrossRef\]](#)
9. Turan, N.G.; Ozgonenel, O. Study of montmorillonite clay for the removal of copper (II) by adsorption: Full factorial design approach and cascade forward neural network. *Sci. World J.* **2013**, *2013*, 342628. [\[CrossRef\]](#) [\[PubMed\]](#)
10. Sengupta, S.; Bhattacharyya, K. Adsorption of heavy metals on kaolinite and montmorillonite: A review. *Phys. Chem. Chem. Phys.* **2012**, *14*, 6698–6723. [\[CrossRef\]](#)
11. Gui, Y.; Shi, J.; Yang, P.; Li, T.; Tang, C.; Xu, L. Platinum modified MoS₂ monolayer for adsorption and gas sensing of SF₆ decomposition products: A DFT study. *High Volt.* **2020**, *5*, 454–462. [\[CrossRef\]](#)
12. Wang, J.; Xia, S.; Yu, L. Adsorption of Pb(II) on the kaolinite (001) surface in aqueous system: A DFT approach. *Appl. Surf. Sci.* **2015**, *339*, 28–35. [\[CrossRef\]](#)
13. Peng, C.; Min, F.; Liu, L.; Chen, J. The adsorption of CaOH⁺ on (001) basal and (010) edge surface of Na-montmorillonite: A DFT study. *Surf. Interface Anal.* **2016**, *49*, 267–277. [\[CrossRef\]](#)
14. Fang, F.; Min, F.; Liu, L.; Chen, J.; Ren, B.; Liu, C. Adsorption of Al(OH)_n⁽³⁻ⁿ⁾⁺ (n = 2–4) on Kaolinite (001) Surfaces: A DFT study. *Appl. Clay Sci.* **2020**, *187*, 105455. [\[CrossRef\]](#)
15. Drits, V.A.; Zviagina, B.B.; Mccarthy, D.K. Factors responsible for crystal-chemical variations in the solid solutions from illite to alu-minoceladonite and from glauconite to celadonite. *Am. Mineral.* **2010**, *95*, 348–361. [\[CrossRef\]](#)
16. Liu, X.; Lu, X.; Wang, R.; Meijer, E.J.; Zhou, H.; He, H. Atomic scale structures of interfaces between kaolinite edges and water. *Geochim. Cosmochim. Acta* **2012**, *92*, 233–242. [\[CrossRef\]](#)
17. Clark, S.J.; Segall, M.D.; Pickard, C.J.; Hasnip, P.J.; Probert, M.I.J.; Refson, K.; Payne, M.C. First Principles Methods Using CASTEP. *Z. Krist. Cryst. Mater.* **2005**, *220*, 567–570. [\[CrossRef\]](#)
18. Segall, M.D.; Lindan, P.J.D.; Probert, M.; Pickard, C.J.; Hasnip, P.; Clark, S.; Payne, M.C. First-principles simulation: Ideas, illustrations and the CASTEP code. *J. Phys. Condens. Matter.* **2002**, *14*, 2717–2744. [\[CrossRef\]](#)
19. Perdew, J.P.; Burke, K.; Ernzerhof, M. Generalized gradient approximation made simple. *Phys. Rev. Lett.* **1996**, *77*, 3865–3868. [\[CrossRef\]](#)
20. Grimme, S. Semiempirical GGA-type density functional constructed with a long-range dispersion correction. *J. Comput. Chem.* **2006**, *27*, 1787–1799. [\[CrossRef\]](#)
21. HMonkhorst, J.; Pack, J.D. Special points for Brillouin-zone integrations. *Phys. Rev. B.* **1976**, *16*, 1748–1749.
22. Du, J.; Min, F.F.; Zhang, M.X.; Peng, C.L.; Liu, C.F. Mechanism of H₂O adsorption on ammonium-illite surface based on density functional theory. *J. China Univ. Min. Technol.* **2017**, *46*, 1349–1356.
23. Churakov, S.V. Ab Initio Study of Sorption on Pyrophyllite: Structure and Acidity of the Edge Sites. *J. Phys. Chem. B* **2006**, *110*, 4135–4146. [\[CrossRef\]](#)

24. Rosso, K.M.; Rustad, J.R.; Bylaska, E.J. The Cs/K exchange in muscovite interlayers: an ab initio treatment. *Clay Clay Miner.* **2001**, *49*, 500–513. [[CrossRef](#)]
25. Lavikainen, L.P.; Tanskanen, J.T.; Schatz, T.; Kasa, S.; Pakkanen, T.A. Montmorillonite interlayer surface chemistry: Effect of magnesium ion substitution on cation adsorption. *Theor. Chem. Acc.* **2015**, *134*, 51–58. [[CrossRef](#)]
26. Peng, C.; Min, F.; Liu, L.; Chen, J. A periodic DFT study of adsorption of water on sodium-montmorillonite (001) basal and (010) edge surface. *Appl. Surf. Sci.* **2016**, *387*, 308–316. [[CrossRef](#)]
27. Liu, X.; Cheng, J.; Sprik, M.; Lu, X.; Wang, R. Surface acidity of 2:1 type dioctahedral clay. *Geochim. Cosmochim. Ac.* **2014**, *140*, 410–417. [[CrossRef](#)]
28. Liu, Y.; Huang, W.; Wei, D. DFT study of interactions between calcium hydroxyl ions and pyrite, marcasite, pyrrhotite surfaces. *Appl. Surf. Sci.* **2015**, *355*, 577–587.
29. Yu, F.-S.; Wang, Y.-H.; Wang, J.-M.; Xie, Z.-F.; Zhang, L. First-principle investigation on mechanism of Ca ion activating flotation of spodumene. *Rare Met.* **2014**, *33*, 358–362. [[CrossRef](#)]
30. Moon, H.S.; Lee, J.H.; Kwon, S.; Kim, L.T.; Lee, S.G. Mechanisms of Na adsorption on graphene and graphene oxide density functional theory approach. *Carbon Lett.* **2015**, *16*, 116–120. [[CrossRef](#)]
31. Ramadugu, S.K.; Mason, S. DFT study of antimony(v) oxyanion adsorption on α -Al₂O₃(1 $\bar{1}$ 02). *J. Phys. Chem. C* **2015**, *119*, 18149–18159. [[CrossRef](#)]